



## Systems design of high performance stainless steels I. Conceptual and computational design

C.E. CAMPBELL\* and G.B. OLSON

*Department of Materials Science and Engineering Northwestern University, Evanston, IL 60208, U.S.A.  
(Tel: 847 491-5221; Fax: 847-491-7820)*

Received and Accepted 2 April 2001

**Abstract.** Application of a systems approach to the computational materials design led to the development of a high performance stainless steel. The systems approach highlighted the integration of processing/structure/property/performance relations with mechanistic models to achieve desired quantitative property objectives. The mechanistic models applied to the martensitic transformation behavior included the Olson–Cohen model for heterogeneous nucleation and the Ghosh–Olson solid-solution strengthening model for interfacial mobility. Strengthening theory employed modeling of the coherent  $M_2C$  precipitation in a BCC matrix, which is initially in a paraequilibrium with cementite condition. The calibration of the  $M_2C$  coherency used available small-angle neutron scattering (SANS) data to determine a composition-dependent strain energy and a composition-independent interfacial energy. Multi-component pH-potential diagrams provided an effective tool for evaluating oxide stability. Constrained equilibrium calculations correlated oxide stability to Cr enrichment in the metastable spinel film, allowing more efficient use of alloy Cr content. The composition constraints acquired from multicomponent solidification simulations improved castability. Then integration of the models, using multicomponent thermodynamic and diffusion software programs, enabled the design of a carburizable, secondary-hardening martensitic stainless steel for advanced bearing applications.

**Keywords:** materials design, case/core systems, martensitic transformation behavior, coherent carbide precipitation, microsegregation, aqueous corrosion resistance

### 1. Introduction

As the cost of experimentation increases and the demand for application specific materials rises, the need to reduce the amount of experimentation in the alloy development process grows. The recent number of efforts to model the composition dependence of materials properties [1-8] reflects this trend. The traditional alloy development process consists of producing numerous heats with systematic composition variations and testing the compositions to discover the alloy with the optimal properties. A computational systems design approach combines mechanistic models of the known processing/structure/property/performance interactions to predict a single alloy composition, which is evaluated for its ability to meet the design goals. With this approach the design goals should be achieved through the iteration of 2 or 3 prototypes; thus, significantly reducing the experimental cost of development. However, to use a systems approach, the relationships between the processing/structure/property/performance interactions must be organized in a manner that recognizes the hierarchical structure of materials [9]. That is, a substructure is present within a given microstructural element, such as the martensitic laths within a packet formed within a prior austenitic grain.

\*Now at NIST, Metallurgy Division, 100 Bureau Dr. Stop 8555 Bldg. 223 A153, Gaithersburg, MD, 20899-8555, U.S.A

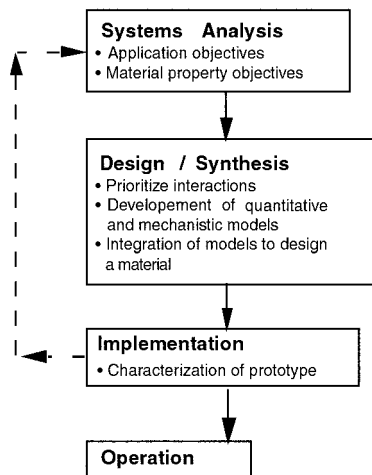


Figure 1. Stages of systems design as applied to materials design.

To organize this hierarchical system of interactions, systems design [10] emphasizes the interaction of the subsystems and the function of the component within the larger system. The four primary steps of systems design are systems analysis, synthesis, implementation, and operation. These steps are outlined in Fig. 1. The first step, systems analysis, requires defining the application and the material property/performance objectives. A flow block diagram is used to clarify the processing/structure/property/performance relations. The first stage of synthesis prioritizes the property objectives and the interactions. After prioritizing, the types of models needed to characterize the interactions and the related subsystems are determined. The required model depends on the priority of the interaction being described. A highly complex model should not be developed to represent an interaction of low priority. Mechanistic based models are preferred for describing interactions of high priority. Once the appropriate models are developed, the models are integrated to design a new material for a specific application. During this design process, it is important not to optimize a subsystem at the expense of the total system. In addition, the design composition should be a robust one: a composition from which small deviations will not result in dramatically different properties. Once the optimal composition is determined, the prototype alloy is made and characterized. Evaluation of the prototype determines whether further modeling of the system is needed or whether continuation to the final step of the design process may be effected: putting the material to use in the intended application.

Application of a systems approach to the design of stainless steels is ideal: there is a wealth of information describing the thermodynamic, mechanical, and corrosion properties of stainless steels and there is a need to double the toughness of the existing highest strength stainless steels. Industrial bearing applications requiring increased toughness and aqueous corrosion resistance range from automotive to nuclear. In addition, the bearing components of the mainshaft of subsonic and supersonic aircraft gas turbines must operate at increasing temperatures, speeds, and loads [11]. The increasing operating temperatures require greater dimensional stability and the increasing engine speeds make raising the fracture-toughness more critical. The low toughness present in current through-hardening alloys makes bearings susceptible to fast-fracture mechanisms that can result in potentially serious secondary damage to the engine. Furthermore, as the desire to improve engine efficiency increases, bearings

increasingly operate in more severe environments, thus requiring improved corrosion resistance. This need to improve corrosion resistance is emphasized by the loss of 50% of the aerospace bearings during storage due to moisture exposure causing corrosion [12].

The research presented here follows a systems approach to the computational design of a high performance stainless steel. This process includes the determination of the desirable property objectives for a new class of stainless steels, the development of the necessary models, the integrated design of a prototype composition, and the characterization of the design prototype. It should be noted that the mechanistic models developed are not limited to use in the design applications of high-performance stainless steels, but can be applied to design applications of other ferrous alloys.

## 2. Conceptual design

### 2.1. PROPERTY OBJECTIVES

Analysis of prototype alloys, bearing steels, secondary-hardening steels, and martensitic stainless steels and of projected industrial needs determined the property objectives for a new class of high performance stainless steels, specifically for aerospace bearings [13]. Achieving the desired high surface hardness and core toughness property objectives, without the use of thermal mechanical processing, requires the use of a case/core system that has two sets of property objectives: one set for the case material and one set for the core material. The development of a case/core system also demands that case/core compatibility always be maintained and that the case and core properties not be optimized at the expense of one another. The properties defining the case include surface hardness, aqueous corrosion resistance, rolling-contact fatigue (RCF) resistance, and wear resistance. The essential core material properties are the toughness and the strength.

The microstructure characteristics controlling the case properties include the surface hardness, the case depth, and the formation of a protective passive film. The surface hardness and case depth determine the fatigue and wear resistance of the case. Cyclic loading of contacting surfaces at low sliding ratios, RCF, results in the initiation of microcracks that form from dislocation accumulation about surface or subsurface defects. RCF failure occurs when the microcracks grow and the stress concentration exceeds the fracture strength of the material. At a fixed applied stress, increases in the Hertzian contact fatigue strength extend the RCF life as the initiation of microcracks is suppressed. The Hertzian contact fatigue strength is proportional to the more easily measured material parameter, material hardness, as shown in Fig. 2. Thus for the currently available aerospace bearing materials, to increase the contact fatigue strength by 15% requires a surface hardness of  $R_C$  65. With this increased surface hardness and a corresponding increase in toughness, an exponential increase in the fatigue life is expected, based on the empirical formulations [14, 15] and experimental work [16, 17]. In addition to maintaining a high surface hardness at room temperature to extend fatigue life, for some applications hot hardness is required due to higher operation temperatures. For such cases, the desired temperature at which the alloy retains a  $R_C$  58 hardness is 400 °C.

To maintain compatibility between the case and the core, the hardness is gradually decreased from a high surface value to a lower core value. The distance over which this decreasing hardness occurs is the case depth. A hardness gradient, which provides critical material strength to exceed the applied stress during RCF, determines the desired case depth. The von Mises stress criterion defines the position of the maximum applied stress within the case.

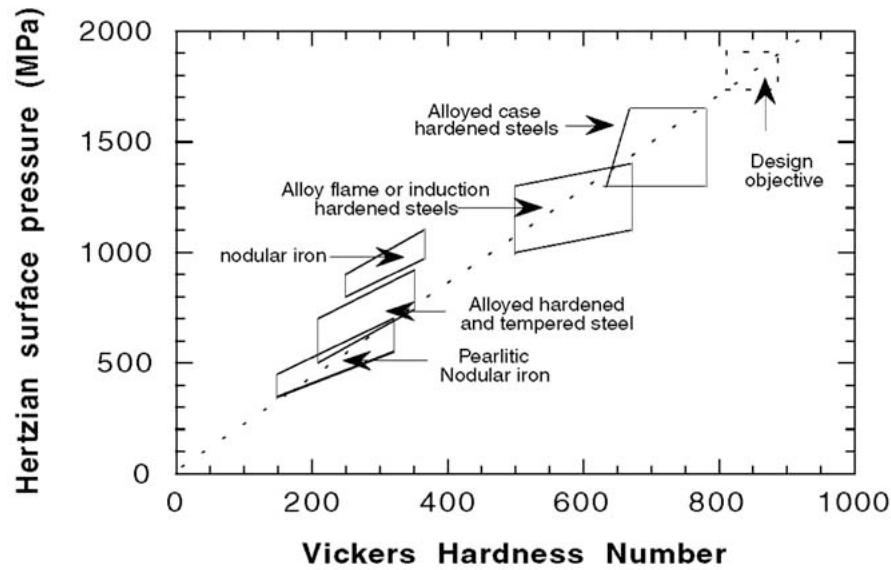


Figure 2. For various ferrous alloys, the contact fatigue strength represented by the Hertzian surface pressure as a function of material hardness, as previously shown in the unpublished work by Breen at the Gear Institute, Evanston, IL, 1992.

Table 1. Compositions of commercial and prototype alloys (Fe is the balance)

Alloy	Weight(%)								
	C	Co	Cr	Mn	Mo	Ni	Si	V	W
52100	0.98–1.10	–	1.30–1.60	0.25–0.45	–	–	0.15–0.30	–	–
M50	0.80–0.85	0.00–0.25	4.00–4.25	0.15–0.35	4.00–4.50	0.00–0.15	0.00–0.25	0.90–1.00	0.00–0.25
M50NiL	0.11–0.15	0.00–0.25	4.00–4.25	0.15–0.35	4.00–4.50	3.20–3.60	0.10–0.25	1.13–1.33	0.00–0.15
HY180	0.11	8	2	0.18	1	10.2	–	–	–
AF1410	0.16	14.25	2.1	–	1.05	10.5	–	–	–
AerMet100	0.24	13.4	3	–	1.18	11	–	–	–
440C	0.95–1.20	–	16–18	1.00	0.75	–	1.0	–	–
Pyrowear 675	0.07	5.4	13.0	0.65	1.80	2.6	0.4	0.6	–
NASA1	0.30	22.5	12.0	–	0.30	8.5	–	0.25	–
NASA2	0.30	25.0	12.0	–	0.30	2.5	–	0.25	–
1605-8A	0.253	15.97	8.97	–	–	4.97	–	–	–
1605-2D	0.25	16	4.1	5	–	–	–	–	–

Wear is the loss or displacement of material due to cyclic loading of contacting surfaces at high sliding ratios. Wear resistance improves with increased dimensional stability and high surface hardness. In comparing the fatigue life and wear resistance of the through-hardening 52100 and the carburizing 8620 bearing alloys, Hengerer et al. [18] found an exponential decrease in weight loss with increasing hardness. (Tables 1 and 2 list the compositions and properties of the alloys described. Optimal fatigue life and wear resistance were achieved with surface hardnesses between  $R_C$  62–64. As wear resistance at high temperatures is also important design objectives include a wear resistance equal to that of the high temperature

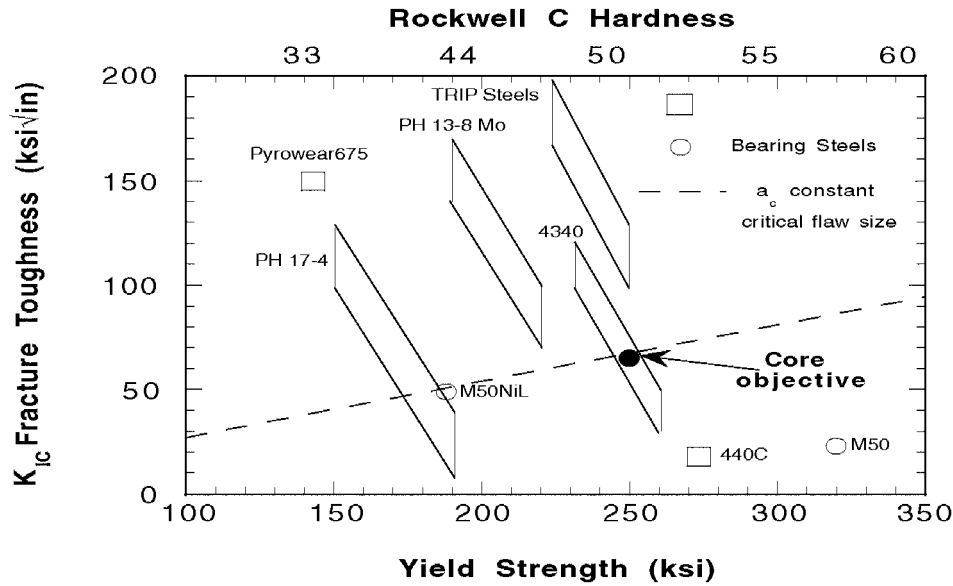


Figure 3.  $K_{IC}$  fracture toughness versus yield strength of stainless steels and reference bearing steels. The dashed line represents the desired critical flaw size.

equivalents of the 52100 and 8620 alloys, through-hardening M50 alloy and the carburizing M50NiL alloy.

The aqueous corrosion resistance should be superior to that of the 440C monolithic stainless bearing alloy, the current standard alloy for high strength applications requiring mild corrosion resistance. Anodic polarization measures the applied potential at which the design alloy and the 440C alloy exhibit a decreased current indicating a transition from the active to passive regions. The decreased current associated with the passive region, due to the increasing oxidizing conditions, results in a lowered corrosion rate. A second evaluation method of the corrosion behavior is salt-spray testing. Despite the reproducibility and correlation limitations of the salt-spray testing, testing in a 5% salt environment provides a simple comparison of material behavior using an industrial accepted standard accelerated corrosion test. It is noted that a corrosion rate of less than  $0.051 \text{ mm yr}^{-1}$  provides 'excellent corrosion resistance,' according to Fontana [19].

The core toughness and strength levels are critical to preventing catastrophic failure. Based on the material selection methods of Ashby [20], Fig. 3 depicts a cross-plot of the yield strength and  $K_{IC}$  fracture toughness properties of existing stainless and bearing steels and reveals the tradeoff between the two properties. The squared ratio of the  $K_{IC}$  fracture toughness over the yield strength is proportional to the critical flaw size, which defines the minimum toughness needed for a given hardness level. For the core material the desired ratio of  $(K_{IC}/\sigma_y)^2$ , equivalent to the non-stainless carburizing bearing steel M50NiL, is 0.185 cm, corresponding to a  $K_{IC} = 65 \text{ MPa}\sqrt{\text{m}}$  ( $60 \text{ ksi}\sqrt{\text{in}}$ ) at a hardness of  $R_C 50$  ( $\sigma_y \approx 250 \text{ ksi}$  ( $1.72 \text{ MPa}$ )). In Fig. 3, the dashed line represents this ratio of  $(K_{IC}/\sigma_y)^2$ .

Table 2. Mechanical properties of commercial and prototype alloys

Alloy	Type	Hardness, $R_C$ Case/Core	Yield strength (MPa)	Fract. Tough. $K_{IC}$ (MPa $\sqrt{m}$ )
52100	Bearing-M	62–65 (core)	345	29
M50	Bearing-M	62	2200	23
M50NiL	Bearing-C	(60–64)/(40–46)	1210	51
HY180	UHS	45	1344	250
AF1410	UHS	48	1650	154
AerMet100	UHS	54.0	1724	126
AerMet100	UHS-Cast	54	1692	125
440C	Stainless-M	57	1896	20
Pyrowear675	Stainless-C	63/40	986	163
NASA1	Stainless-N	70/58	–	47
NASA2	Stainless	40	–	32

M = Martensitic, C = Carburizing, N = Nitriding, UHS = Ultrahigh-strength.

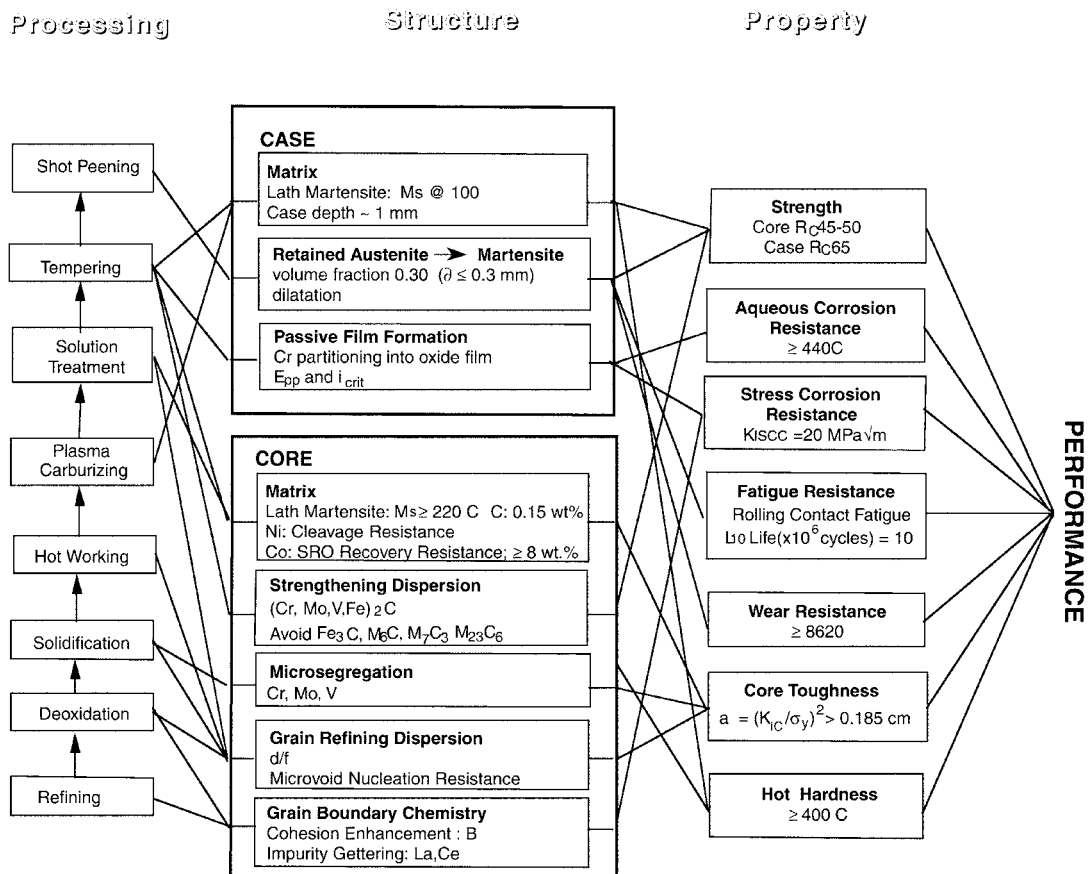


Figure 4. Flow-block diagram of the processing/structure/property/performance interactions for a carburizing, secondary-hardening, martensitic stainless steel.

## 2.2. DESIGN APPROACH

These property objectives are achieved by a structure of hierarchical interacting microstructural subsystems. The flow block diagram in Fig. 4 illustrates the interactions among the desired hierarchical microstructural subsystems required for the processing and the property objectives. Of the two major microstructural subsystems, the case and core subsystems, the case microstructure is the more complex subsystem having to provide strength, corrosion resistance, and fatigue resistance. The primary function of the core subsystem is to provide fracture-toughness.

### 2.2.1. Case subsystem

The desired high strength and aqueous corrosion resistance case properties require the carburization of a lath martensitic matrix microstructure. The lath microstructure produced after quenching from the solution treatment temperature has a high dislocation density that provides a direct strengthening contribution, as well as nucleation sites for a fine-scale precipitate dispersion. The carburization of the case material within the limits of the carbon solubility in the FCC phase field increases the strength of the martensitic matrix by increasing the strain dilation in the matrix with the carbon occupation of interstitial sites. If the carburization is done in the single phase FCC field, the gradient carbon concentration results in a beneficial compressive stress profile. If carburization occurs outside the single FCC phase field, primary carbides may form interfacially and act as sites for crack initiation. In addition the formation of primary carbides removes Cr from the matrix decreasing the aqueous corrosion resistance. Preliminary results of notch-fatigue testing by Kuehmann [21] and rolling contact fatigue testing by Wise [22] indicate the effectiveness of reducing the primary carbide fraction to increase the fatigue life.

Precipitation of fine-scale  $M_2C$  (HCP,  $M = Cr, Mo, V, Fe$ ) carbides using secondary hardening further reduces the interparticle spacing and thus increases the strength. During secondary-hardening (stage IV tempering),  $M_2C$  carbides precipitate heterogeneously on dislocations and produce a fine-scale dispersion [23]. To maintain the initially nucleated small particle size requires precipitation in a highly supersaturated solution, which fosters nucleation and coarsening without growth. Langer and Scharwitz [24] and Kampmann and Wagner [25] demonstrated the effectiveness of this type precipitation in maintaining the initial particle size. An additional mechanism to improve the strength dictates maintaining the dislocation substructure of the martensitic microstructure at the secondary hardening temperatures. Speich [26] determined that this can be achieved with a matrix composition containing at least 8 wt.% Co.

Formation of a passive film on the surface of the case material supplies the needed aqueous corrosion resistance for the alloy. This passivating film is primarily composed of  $Me_2O_3$  ( $Me = Cr, Fe, Ni$ ) and  $Me_3O_4$  oxides; therefore, the amount of Cr partitioning to the film controls the formation and stability of the film. Experiments by Kirchhiem and co-workers [27, 28] in Fe-Cr alloys determined the amount of Cr in the oxide film is logarithmically dependent on the matrix Cr concentration. Their work supports the conclusion that the corrosion resistance for an alloy with a fixed Cr content can be improved by increasing the activity of Cr in the matrix, and thus, promoting Cr partitioning to the oxide film. Therefore, the design parameters to improve the aqueous corrosion resistance focus on decreasing the fraction of precipitated carbides, which decrease the matrix Cr concentration, and on increasing the activity Cr in the matrix to enhanced the partitioning of Cr to the oxide film.

### 2.2.2. *Core subsystem*

The following constituents control the fracture toughness: the matrix Ni composition, the prior austenite grain size, the martensitic microstructure, the reduction of microvoid nucleation sites, and the grain boundary cohesion. Optimization of these constituents yields ductile fracture at room temperature; that is shifting the ductile-to-brittle transition (DBT) temperature below room temperature. Early work [29] showed additions of 1 wt. % Ni to ferrous alloys have effectively reduced the DBT temperature below room temperature and the same behavior was observed in low strength binary Fe-Ni alloys by Jolley [30] and Leslie [31]. Sufficiently decreasing the prior austenitic grain size also aids in shifting the DBT to below room temperature. This desired reduction of the grain size is achieved by using Ti carbide (Ti,Mo)C,N grain refiners (with diameters between 10 nm and 180 nm) [32] and by optimizing the solution temperature to achieve high hardness with the minimum solution treatment time. The beneficial effects of refining the solution temperature have been demonstrated for the AF1410 [33] and AerMet100 [34] alloys.

The lath martensitic microstructure formed within the prior austenite grains provides an essential microstructural element for obtaining both high strength and toughness. The fine-scale lath microstructure produced after quenching is dependent on the martensitic start,  $M_s$ , temperature, which is composition dependent. Experimental observations showed that an  $M_s$  temperature above 150 °C is required to obtain a lath microstructure upon quenching from the solution treatment temperature. As the  $M_s$  temperature decreases the fraction of retained austenite increases and lath microstructure coarsens to a plate-like microstructure. Thus, the first step in controlling the type of martensitic microstructure formed is to determine the composition dependence of the  $M_s$  temperature.

In corrosive environments where chemical embrittlement can occur, grain boundary cohesion also becomes important factor in maintaining toughness. The segregation of impurities to grain boundaries results in brittle-fracture as impurities lower the interfacial cohesion. For a grain boundary with a given impurity, Rice and coworkers [35] modeled the competition between crack-tip blunting by dislocation emission and brittle interfacial cleavage. The model predicts that ductile fracture will prevail if the energy for dislocation emission is greater than the Griffith work for interfacial cleavage controlled by interfacial thermodynamics. The results of literature thermodynamic data [36] confirmed the detrimental effect of phosphorus, tin, antimony and sulfur. Boron was shown to be a superior cohesive enhancer, as supported by first-principles electronic calculations [1]. Detrimental impurities can be removed from the grain boundaries using gettering techniques [37–40]. Watton et al. demonstrated that lanthanum and cesium can be used to effectively getter both P and S impurities [41].

For the integrated design of a case/core material, the system of interactions between the desired properties, structure, and processing is depicted in Fig. 4. Following a systems approach, the next step is defining the priorities of the processing/structure/property interactions and identifying the conflicting objectives of the various subsystems. The case properties are the primary property objectives, while the core properties are secondary objectives. These case property objectives correspond to the following microstructural and processing objectives: a quench-hardenable lath martensitic matrix microstructure, the formation of a passivating film at the surface, and the avoidance of primary carbides. Secondary microstructural objectives include the efficient use of secondary hardening to optimize the strength and toughness and the reduction of microsegregation during solidification.

Within this system, conflicting objectives exist. The  $M_s$  temperature is controlled primarily by the C, Co, Cr, and Ni levels. Co additions increase the  $M_s$  temperature, while increasing the C, Cr, and Ni compositions strongly decreases the  $M_s$  temperature. Maintaining a constant  $M_s$  temperature by limiting C conflicts with the desired strength objectives, which require high carbon. Aqueous corrosion resistance depends on increasing the Cr that partitions to the oxide film; however, increasing Cr lowers the  $M_s$  temperature and promotes undesirable carbides.

Within the interactions of the secondary objectives are other conflicting objectives. Vanadium increases the driving force for precipitation of the coherent  $M_2C$  carbide; however, V solubility at the solution treatment temperature,  $T_s$ , is limited. Increasing the amounts of carbide formers, Cr, Mo, and V increases the tendency for solidification microsegregation. The tempering process increases the strength via secondary-hardening, but can promote the relaxation of desired residual compressive stresses.

### 3. Model development

Based on the priorities of the property objectives, the models developed emphasize the martensitic transformation behavior, the precipitation of coherent  $M_2C$  carbides, the formation and stability of passivating oxide films, and the microsegregation occurring during solidification processing. These models correlated the desired microstructural features and processing conditions with thermodynamic quantities and diffusional reactions using the Thermo-Calc [42] and DICTRA [43] software platforms. The application of these models to the current design application is now described. However, for details regarding the specific models, the reader is encouraged to consult the literature.

#### 3.1. MARTENSITIC TRANSFORMATION BEHAVIOR

The FCC→BCT martensitic transformation, which occurs upon quenching from the solution temperature to room temperature, exhibits a high strength matrix. This displacive diffusionless transformation results in a large distortion strain and a high dislocation density. The strain energy associated with the large lattice deformation dominates the kinetics and morphology of the transition. To achieve the desired lath morphology requires a  $M_s$  temperature of approximately 150 °C and thus, the modeling objective is to determine the composition dependence of the  $M_s$  temperature.

Using Thermo-Calc, the  $M_s$  temperature for a multicomponent ferrous-based alloy was predicted implementing the Olson–Cohen model [44, 45] for heterogeneous nucleation and the Ghosh–Olson solid-solution strengthening model [46, 47] for the description of the frictional work associated with interfacial motion. Recognizing the considerable uncertainty in the thermodynamics of carbon ordering in the BCT martensite, the chemical thermodynamics of the system were modeled using the descriptions of the FCC and BCC solid solutions based on the SGTE Solution database [48]. Modifications to the SGTE description were made by Ghosh (unpublished thermodynamic assessment work done by G. Ghosh at Northwestern University, Evanston, IL, 1992) and by Campbell [13], which incorporate Fe-Co-Cr ternary interaction parameters based on the evaluation of model ternary alloys. For a wide range of temperatures and compositions, the predicted  $M_s$  temperatures correlate well with the measured  $M_s$  temperatures, Fig. 5. The standard deviation of the difference between the measured and calculated  $M_s$  is  $\pm 35$  °C. Several prototype and commercial alloys were used to test the validity of the model. All of the commercial alloys show good agreement with the model. In

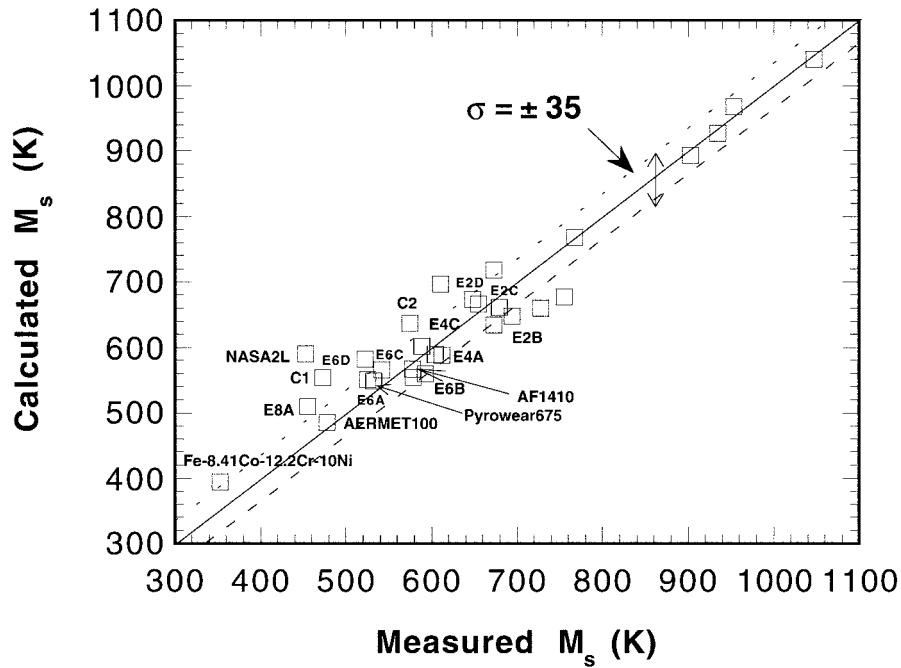


Figure 5. Correlation of the calculated and measured  $M_s$  temperatures for model and commercial alloys.

particular, the deviation for the commercial carburizing stainless steel Pyrowear 675 and a stainless prototype (E8A) is  $\pm 25$  °C. These alloys demonstrate the success of the model to predict the martensitic behavior in high Co-Cr ferrous alloys.

### 3.2. PRECIPITATION OF COHERENT $M_2C$ CARBIDES

The efficiency of the strengthening dispersion is determined by the critical particle size and the interparticle spacing. Characterization of the AF1410 alloy [49–51] demonstrated the effectiveness of the precipitation of coherent  $M_2C$  carbides in a highly supersaturated BCC matrix. This precipitation in a highly supersaturated BCC matrix resulted in the suppression of the growth regime leading to precipitation by a coarsening process, as predicted by the Langer–Schwartz model [24, 25, 52], and thus, the mean carbide size remained near the critical particle size,  $r^*$ , which smoothly increased as the supersaturation dropped. Modeling of the critical particle size as a function of the fraction of the precipitation reaction completed uses the Gibbs–Thompson equation (1) and small angle neutron scattering (SANS) carbide size data for the AF1410 [50] and model alloys (unpublished research by P. Jemian and J.R. Weertman, Northwestern University, Evanston, IL, 1992).

$$r^* = \frac{2\gamma}{\Delta G}, \quad (1)$$

where  $\gamma$  is the interfacial energy ( $\text{J m}^{-2}$ ) and  $-\Delta G$  is the precipitation driving force ( $\text{J m}^{-3}$ ) associated with the supersaturation level. The modeling efforts require that the initial state from which precipitation initiates be defined and the free energy of the coherent  $M_2C$  carbide phase be described.

In the tempering temperature range of 400 °C to 550 °C the carbon mobility is much greater than that of the substitutional elements and results in the initial precipitation of paraequilibrium cementite, which only requires carbon diffusion [53–56]. With additional tempering time, diffusion of metallic substitutional elements occurs and  $M_2C$  carbides precipitate, dissolving the cementite. The BCC-cementite paraequilibrium conditions assume equal carbon chemical potentials and no redistribution of the substitutional species:

$$\mu_C^{\text{CEM}} = \mu_C^{\text{BCC}} \sum_i y_i (\mu_i^{\text{CEM}} - \mu_i^{\text{BCC}}) = 0 \quad \text{where } i \neq C \quad (2)$$

where  $\mu_C^{\text{CEM}}$  is the carbon chemical potential in cementite and  $\mu_C^{\text{BCC}}$  is the carbon chemical potential in BCC. For the current thermodynamic description, the substitutional species (Fe, Cr, Co, Mo, Ni, and V) and the interstitial species (C and vacancies) are modeled on separate sublattices and thus,  $y_i$  is the site fraction of  $i$  on its corresponding sublattice. As there is no substitutional diffusion,  $y_i^{\text{CEM}} = y_i^{\text{BCC}}$  where  $i$  does not equal carbon. The chemical potentials of the substitutional species in the BCC and cementite phases are given by  $\mu_i^{\text{BCC}}$  and  $\mu_i^{\text{CEM}}$ , respectively. Experiments confirmed that this paraequilibrium condition is the initial state from which  $M_2C$  carbide precipitation begins [57].

The free energy of the coherent  $M_2C$  carbides is the summation of the chemical free energy, the elastic energy, and the interfacial energy.

$$G_m^{\text{M}_2\text{C}} = G_{\text{chemical}} + G_{\text{elastic}} + G_{\text{interfacial}} \quad (3)$$

The HCP phase description of the SGTE solution database [48] is used to describe the chemical thermodynamics of the  $M_2C$  carbide. The linear-elastic model for an inhomogeneous inclusion treated by Liang [58] and King et al. [59] represents an upper bound on the composition-dependent elastic energy. It has been assumed that the upper bound estimate of the elastic self-energy scales by a fixed correction factor and is independent of carbide phase fraction at the low fractions of interest. The interfacial energy is assumed to be composition and size independent for a given state of coherency. The model of Johnson and Cahn [60] describes the shape dependence of the capillary energy employing the experimental observations of the  $M_2C$  carbides size and shape. The fraction of linear-elastic energy and interfacial energy were calibrated using SANS data from the AF1410 alloy [51] and other model alloys.

Calibration with the SANS data determined an elastic energy correction factor of 0.3 for the fully coherent state [13]. A three coherency state model was necessary to fit the data, with full coherency below a 30 Å particle size diameter, a semicoherent state between 30 Å and 50 Å, and an incoherent state above 50 Å. The interfacial energy associated with the coherent particles is 120 mJ m<sup>-2</sup>, with semicoherent particles is 404 mJ m<sup>-2</sup>, and with incoherent particles is 520 mJ m<sup>-2</sup>. With these calibrations, the Gibbs-Thompson equation predicts the mean particle size as a function of the precipitation reaction completed [13]. Fig. 6 shows the correlation of the calibrated model predictions of the evolution of the shape-corrected effective particle size with the experimental measurements. Thus, the  $M_2C$  strengthening is optimized by maximizing the driving force for coherent  $M_2C$  carbides precipitating in the BCC matrix in paraequilibrium with cementite. Maximizing the driving force decreases the particle size and increases the strength.

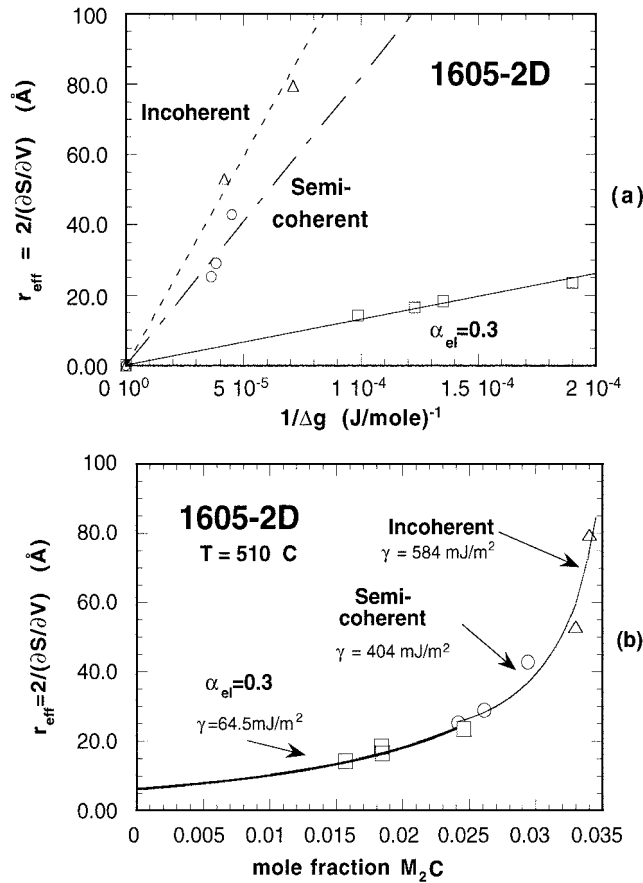


Figure 6. For alloy 1605-2D at 510 °C (a)  $r_{\text{eff}}$  versus  $1/\Delta G$  for coherent  $\alpha_{\text{el}} = 0.3$  (□), semi-coherent M<sub>2</sub>C with C in paraequilibrium with cementite (O), and incoherent M<sub>2</sub>C with C in BCC-M<sub>2</sub>C equilibrium (Δ). (b)  $r_{\text{eff}}$  as a function of mole fraction of M<sub>2</sub>C. The data symbols in (b) correspond to the fit used in (a).

### 3.3. AQUEOUS CORROSION RESISTANCE

The pH-potential diagrams for multicomponent alloys and constrained equilibrium calculations determining the degree of Cr partitioning to the oxide film were used to optimize the aqueous corrosion resistance. The pH-potential diagrams, as demonstrated by Pourbaix [61], represent the equilibrium phase boundaries within dimensions of pH and applied potential for the given solid phases and the aqueous solution. Originally Pourbaix [61] assumed dilute solution concentrations with the range of 1.0e-4 molal to 1.0e-6 molal. The pH-potential diagram calculations for multicomponent alloys assume a total ionic concentration less than 1.0e-4 molal in the aqueous solution and that the ionic concentration of the solution scales with base alloy composition. The latter assumption is based on the work of Kirchheim [28]; study of the passivation of Fe-Cr alloys at long times (steady-state conditions) revealed that the relative Cr concentration of the electrolyte solution was approximately equal to the Cr composition of the base alloy. The pH assumed in the pH-potential diagram calculation is the pH at the metal/film interface. However, when comparing to experiments typically the referenced pH is the bulk pH, even though the bulk pH may differ substantially from the interface pH. This

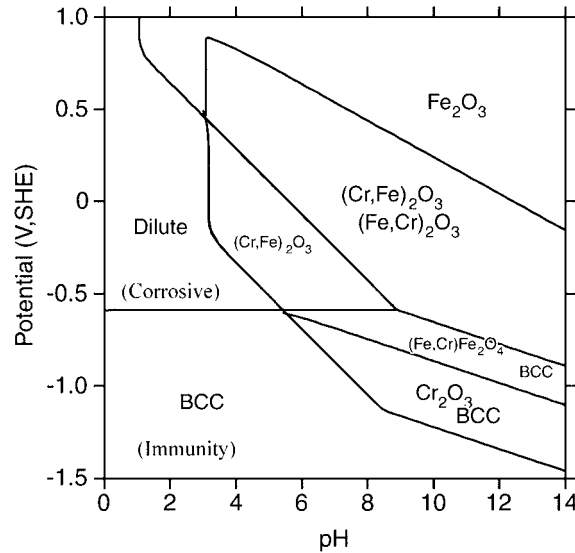


Figure 7. pH-potential diagram for Fe-12Cr considering non-stoichiometric oxides.

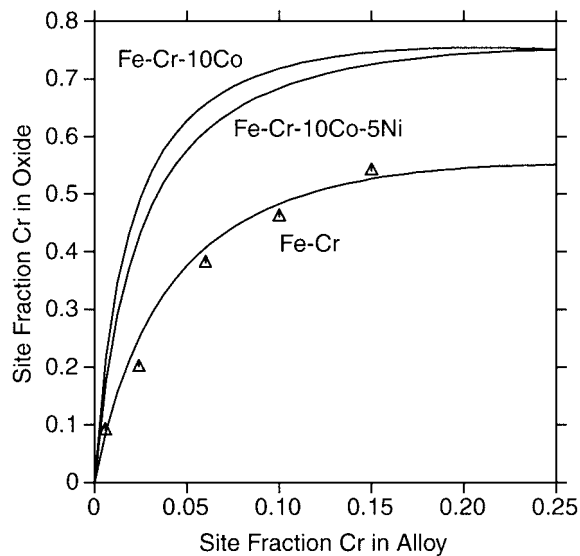


Figure 8. Calculation of Cr partitioning in the metastable spinel phase ( $\text{Me}_3\text{O}_4$ ). A strain term of 50 kJ/mole is added to the terms describing the  $\text{Fe}^{+3} - \text{Cr}^{+3}$  exchange on the octahedral sublattice. The  $\Delta$  symbols represent the experimental work of Kirchiem [28].

inconsistency occurs due to the many difficulties associated with measuring the interface pH [62].

Figure 7 is the calculation of the pH-potential diagram for a Fe-12Cr (wt.%) alloy in a water-based aqueous solution assuming non-stoichiometric multicomponent oxide phases. The addition of Cr shifts the passive boundaries to lower pH levels, thus increasing the region over which the passivation occurs. The pH-potential diagrams for multicomponent alloys can be used to indicate whether the desired oxide passivation is thermodynamically favored.

To determine if the desired passivation occurs requires kinetic modeling. A constrained metastable equilibrium calculation is used as a first order approximation of the dynamic state. A strained-layer model with composition dependent strain energy terms based on the coherent  $M_2C$  model [58, 59] was developed to calculate the constrained equilibrium between the metal alloy and the initial forming spinel-type oxide,  $(Fe,Cr)_3O_4$ . The model strain energy terms were calibrated to the observed amount of Cr partitioning to the oxide film. Fig. 8 shows the calibration of the Cr partitioning to the data of Kirchheim [28] and the application of the model to high order systems, which fosters more efficient partitioning.

#### 3.4. SOLIDIFICATION MICROSEGREGATION

As a large amount of solidification microsegregation was associated with an earlier stainless prototype (NASA2) and the AerMet100 alloy was characterized to have acceptable levels of microsegregation, a method to predict an degree of microsegregation in an alloy was developed using the DICTRA software and calibrating the calculations with the experimental measurements from the AerMet100 alloy [63]. The DICTRA simulation of solidification assumes equilibrium is maintained at the liquid/solid interface and diffusion occurs in both the solid and liquid phases. The simulation also assumes that initial liquid composition is homogeneous and the liquid/solid interface is planar. For each time increment, the flux equations are numerically solved along each point of the geometric grid subdividing the assumed symmetrical dendrite.

DICTRA simulations of the AerMet100 solidification process show good agreement with the measured microsegregation after solidification [63]. Comparison of the composition profiles, Fig. 9, shows that the thermodynamic and kinetic parameters used produced quantitative results, which require no further calibration. Thus, solidification simulations for secondary-hardening ferrous alloys can be used to determine compositions that minimize microsegregation.

### 4. Computational design integration

To complete the synthesis step of systems design (Fig. 1), the design models were integrated to predict an optimal composition to meet the previously established objectives. Fig. 10 illustrates the thought process guiding the integration of the models.

#### 4.1. MATRIX OPTIMIZATION

The first step in the design of a carburizing, secondary-hardening, martensitic stainless steel is to estimate the carbon content needed to achieve the desired core and case strengths. The strengthening predictions [22] give some guidance to the strength achieved for a given carbon level. The predictions assume that a given alloy composition dictates a specific carbide volume fraction and considers carbides of fixed particle diameter. Based on these assumptions, a modified version of Orowan [64] and Ashby [65] theory predicts the strength.

$$\Delta\tau_{\text{Total}} = \Delta\tau_{\text{bypass}} + \Delta\tau_{\text{BCC}} \quad (4)$$

$$\Delta\tau_{\text{bypass}} = 1.88 \frac{Gb}{2\pi(1-\nu)^{1/2}L} \ln\left(\frac{2R}{b}\right) \quad \text{where} \quad L = R\left(\frac{2}{f}\right)^{1/2}$$

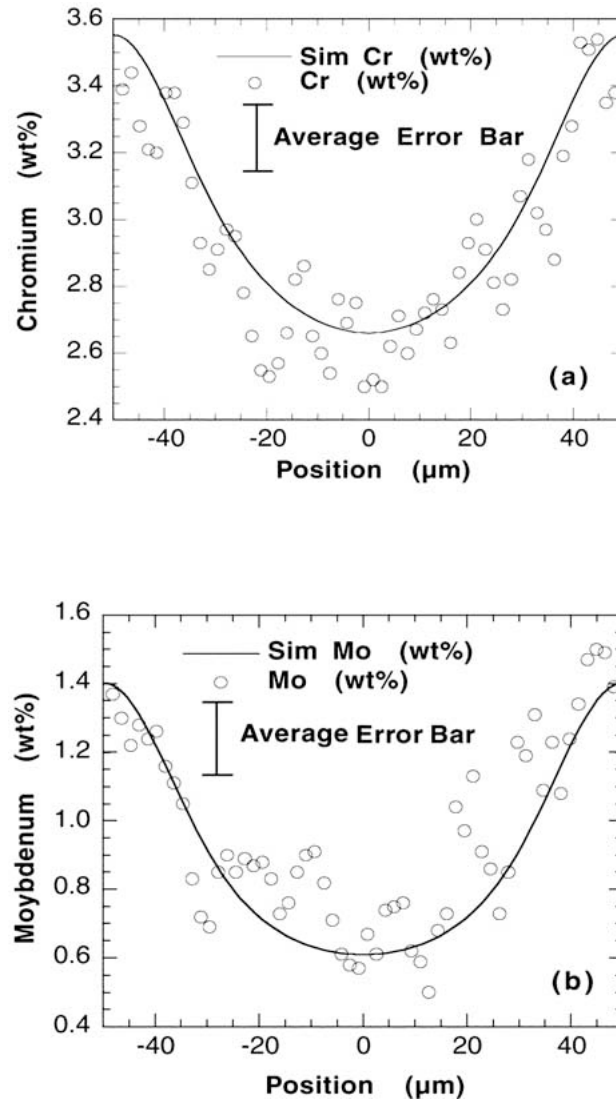


Figure 9. For the as-cast AerMet100, experimental and DICTRA simulated composition profiles across a 100  $\mu\text{m}$  secondary dendrite arm for (a) Cr and (b) Mo.

and where  $\Delta\tau_{\text{BCC}}$  is the estimated martensite matrix strength, 155 VHN,  $G$  is the BCC shear modulus,  $\nu$  is Poisson's ratio for the matrix,  $R$  is the particle radius,  $b$  is the Burger's vector, and  $f$  is the carbide volume fraction. Figure 11 depicts the predicted hardness as a function of carbon for given carbide particle sizes and provides an estimate of the desired carbon composition. The positions of the hardness values for the AF1410 and AerMet100 alloys are consistent with the SANS measurements of the particle size [50]. The higher driving force associated with the NASA1 prototype predicts a smaller particle size; the measured hardness is consistent with a particle size of 40  $\text{\AA}$ . Assuming a precipitation driving force equivalent to NASA1 can be obtained to achieve the same particle refinement, for a  $R_c$  65 case hardness and a  $R_c$  50 case hardness the estimated carbon compositions are 0.5 wt.% C in the case and 0.2 wt.% C in the core.

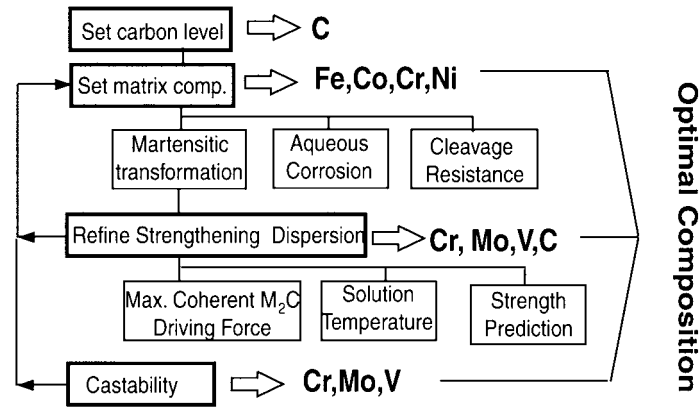


Figure 10. Schematic of the design optimization procedure.

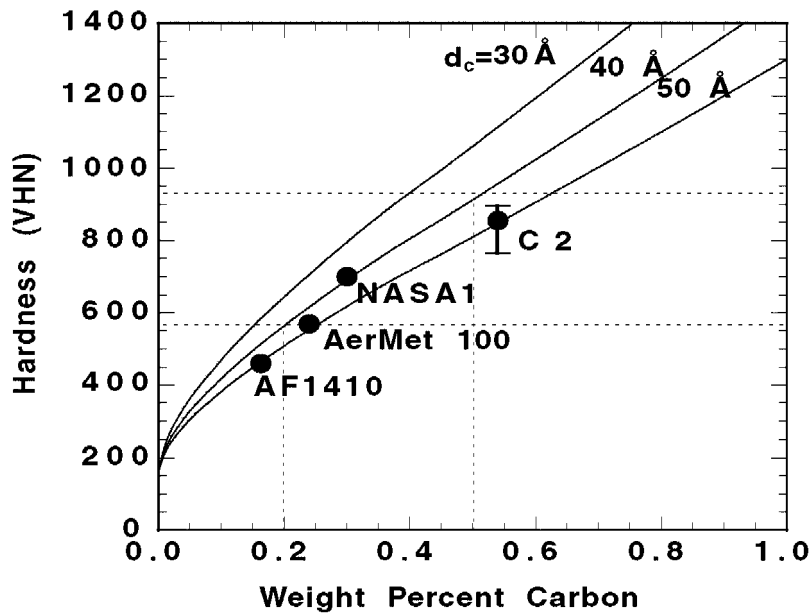


Figure 11. Hardness as a function of alloy carbon content [22]. The dashed lines represent the desired case and core carbon and the corresponding hardness levels at 40 Å particle size.

With these carbon content estimates, the matrix composition in both the case and the core is optimized to achieve the correct  $M_s$  temperature gradient, aqueous corrosion resistance, and sufficient cleavage resistance in the core material. As previously indicated the desired  $M_s$  temperature needed to achieve a lath martensitic microstructure is 150 °C; thus, the desired minimum case  $M_s$  temperature is 150 °C. The desired core  $M_s$  temperature is chosen to be 100 deg higher than the case  $M_s$  temperature to establish a reasonable  $M_s$  temperature gradient, which will correspond to the desired carbon gradient and will provide a compressive stress profile at the surface. However, the core  $M_s$  temperature is not a primary objective and the temperature gradient may be altered to accommodate objectives with higher priority. In addition, to compensate for error in the  $M_s$  model for high Co-Cr compositions the design  $M_s$

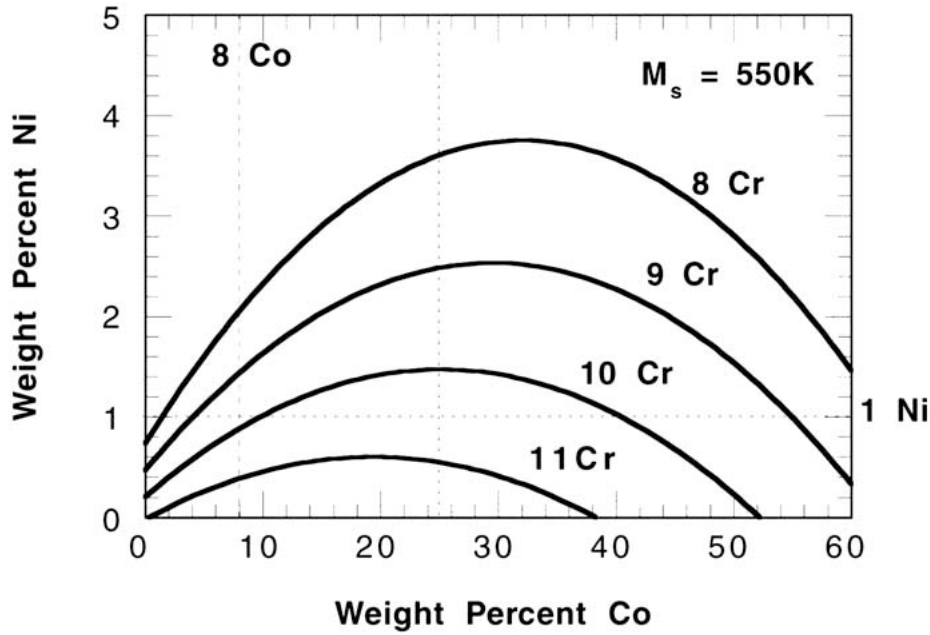


Figure 12. Constant  $M_s$  contours at 550 K defining the Co and Ni content of the matrix. The dashed lines represent the system constraints.

values are raised approximately 25 deg. Thus, the matrix core composition is optimized with respect to constant  $M_s$  contours at 550 K (277 °C) as functions of Co and Ni compositions at various Cr levels, as shown in Fig. 12. The contours have a parabolic shape for which the maximum Ni content shifts to lower Co levels as the Cr content increases. However, the benefits of short-range order dislocation recovery resistance require at least 8 wt.% Co [26]. Ni contents greater than 1 wt.% Ni shift the DBT temperature below room temperature improving the fracture toughness resistance. Cost constraints suggest limiting the Co content to less than 25 wt.%. The constraints on the Ni and Co compositions, represented by the dashed lines in Fig. 12, limit the Cr composition to 10 wt.% Cr or less. The optimization of the aqueous corrosion resistance also influences the matrix Cr composition, and this will be discussed further in the re-optimization of the composition. The high Co contents of interest (15 wt.%–20 wt.%) promote the partitioning of Cr to the oxide film increasing the oxide stability, as seen in Fig. 8.

The carbon gradient resulting from carburizing and the corresponding  $M_s$  temperature gradient limit the optimum Ni content. For various Ni concentrations, Fig. 13 represents the  $M_s$  gradient as the C increases from the core to the case. The compositions of Ni and C that produce a  $M_s$  of 450 K (177 °C) in the case are chosen. Finally, the Ni and Co contents were refined once more using the 9Cr  $M_s$  contour at 450 K, Fig. 14. The broad maximum suggests there is little benefit derived from increasing the Co from 15 wt.% to 20 wt.%. Thus matrix composition is fixed at Fe-15Co-1.5Ni-9Cr-0.2C (0.5C case) wt.%.

#### 4.2. STRENGTHENING DISPERSION OPTIMIZATION

With an initial matrix composition set, refinement of the secondary hardening dispersion maximizes the strength. At the assumed tempering temperature of 482 °C, the coherent  $M_2C$

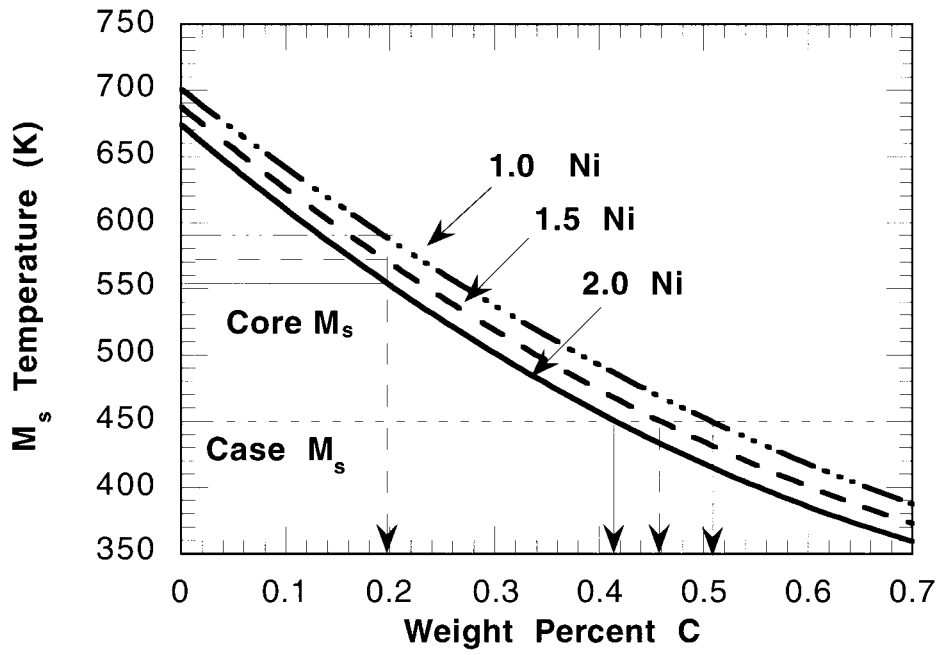


Figure 13.  $M_s$  temperature as a function of matrix carbon content for Fe-15Co-9Cr-Ni (wt.%) alloys. The dashed lines represent the case and core  $M_s$  temperatures corresponding to the various Ni and C compositions. The core C composition is fixed at 0.2 wt.% C and the case  $M_s$  temperature is fixed at 450 K.

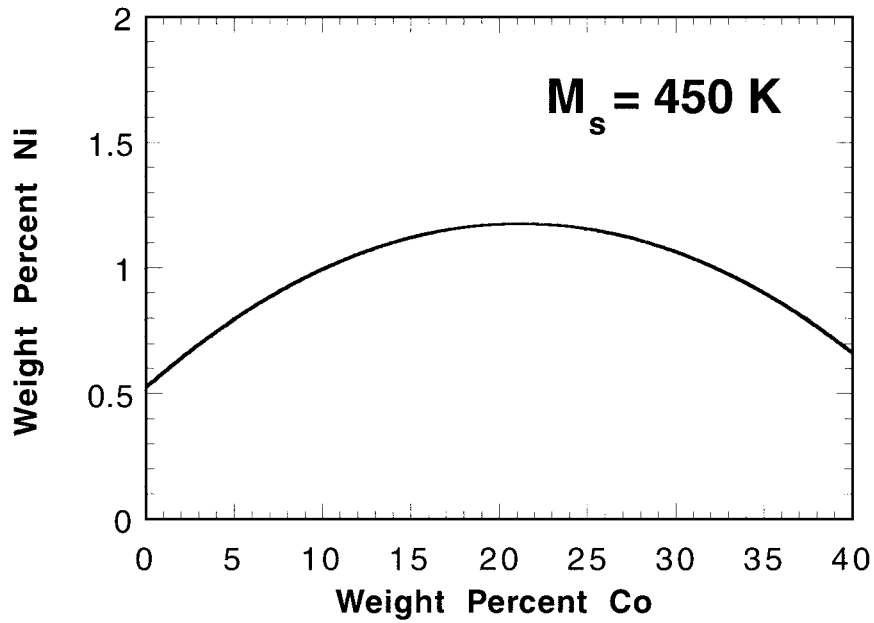


Figure 14.  $M_s$  contour at 450 K defining the case matrix composition for the Fe-Ni-Co-9Cr-0.5C (wt.%) system.

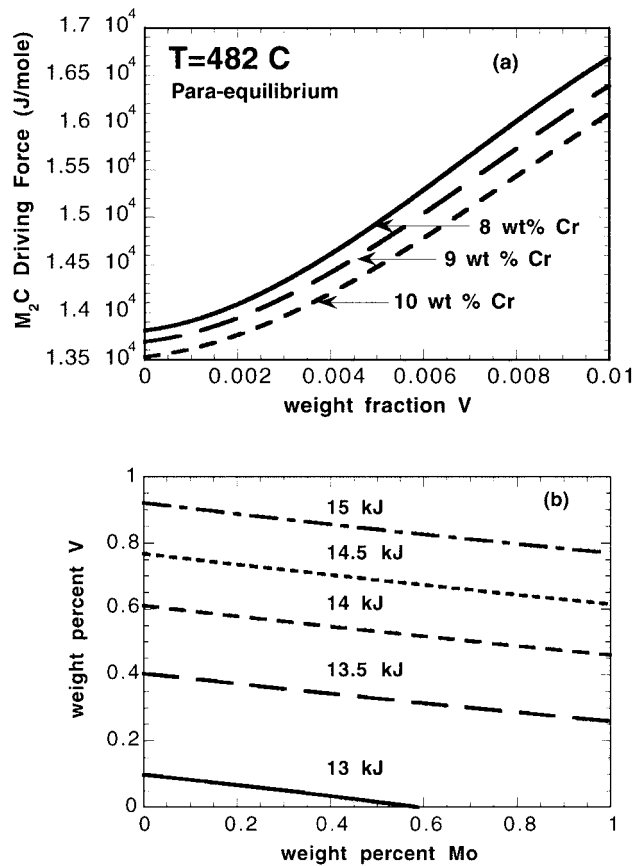


Figure 15. Composition dependence of the coherent  $M_2C$  driving force, calculated assuming the initial conditions are BCC-cementite paraequilibrium at 482 °C (a) Fe-15Co-1.5Ni-Cr-0.5Mo-V-0.5C (wt.%) (b) Fe-15Co-1.5Ni-9Cr-Mo-V-0.48C (wt.%).

driving force is maximized, within the composition constraints of the solubility at the solution temperature ( $< 1100$  °C). In addition to these composition constraints, the paraequilibrium conditions between BCC and cementite restrict the amount of carbon in the matrix decreasing the  $M_2C$  driving force. For both the core and case compositions, the design calculates the coherent  $M_2C$  driving force under paraequilibrium conditions using the coherent  $M_2C$  model. The  $M_2C$  coherency model assumes a carbide aspect ratio of 1, appropriate to initial nucleation. To insure sufficient driving force to obtain the desired strengthening, the driving force for the new alloy should equal the driving force of a prototype alloy with sufficient hardness, NASA1, which has a driving force of 15.9 kJ/mole at the tempering temperature of 455 °C. Figure 15 explores the composition dependence of the coherent  $M_2C$  driving force with respect to the Fe-15Co-9Cr-1.5Ni-0.48C matrix, assuming a tempering temperature of 482 °C. Both Mo and V increase the driving force, while increased Cr decreases the driving force.

The carbon-vanadium section at 1100 °C, seen in Fig. 16, shows the constraints imposed on the V composition. To avoid primary carbides, the material must be solution treated in the single FCC phase field. To achieve a solution treatment temperature of 1100 °C for both the

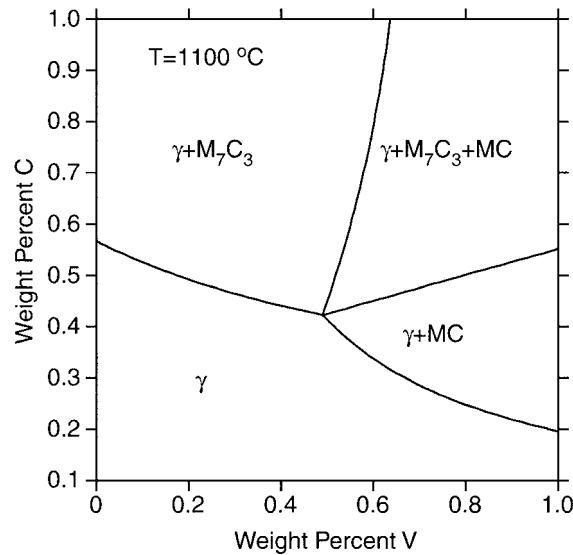


Figure 16. Phase section at 1100 °C with respect to C-V in the Fe-15Co-1.5Ni-9Cr-0.5Mo-V-C (wt.%) system, calculated using the SGTE database.

core and case restricts the V composition to 0.2 wt.% V and the case carbon level to 0.48 wt.% C.

#### 4.3. AQUEOUS CORROSION

Thermodynamics are needed to predict the formation of a passive film on the surface, the increase of Cr activity in the matrix, and the avoidance of primary carbides. For a 9 wt.% Cr addition, the pH-potential diagram indicates that the passivating oxides  $\text{Me}_3\text{O}_4$  and  $\text{Me}_2\text{O}_3$  are thermodynamically stable. The additional Co in matrix increases the Cr activity in the matrix and correspondingly increases the partitioning ratio of Cr, as shown in Fig. 8. Based on the work of Kirchheim [28], this increase in Cr activity should improve the kinetics for the formation of the  $\text{Me}_3\text{O}_4$  oxide film. Using the fine scale secondary-hardening  $\text{M}_2\text{C}$  carbides and following processing schedules that do not include phase fields in which primary carbides are thermodynamically stable prevents the depletion of matrix Cr needed for the formation of a passive film.

#### 4.4. CASTABILITY

Efforts to improve castability constrain the molybdenum concentration. The castability of the alloy improves by decreasing the microsegregation and by improving the fluidity through a reduced freezing range [66]. The fluidity, the ability to fill a mold, is greatest when freezing occurs at a constant temperature allowing the slow inward growth of solid metal. Large freezing ranges result in the liquid surrounding interlacing dendrites (i.e. the metal is in a mushy condition), which restricts the flow of the liquid. The dependence of fluidity on the freezing range was verified in a study of aluminum alloys with similar solidification characteristics [67].

The segregation ratios,  $\delta = C_{\text{max}}/C_{\text{min}}$  ( $C = \text{concentration}$ ) characterizes the microsegregation after solidification. Diffusion simulations of the solidification process allow the mi-

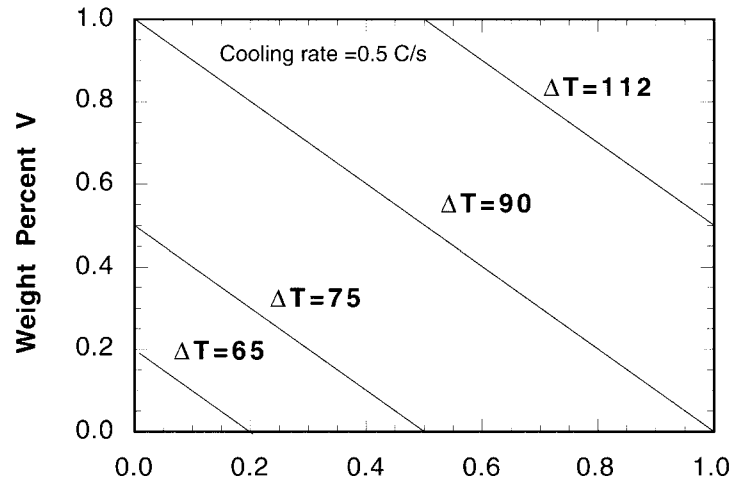


Figure 17. Contours of constant freezing ranges in the Mo-V composition space for Fe-9Cr-Mo-V-0.2C (wt.%) alloys. A cooling rate of  $0.5\text{ }^{\circ}\text{C s}^{-1}$  and no carbide precipitation were assumed.

croseggregation occurring in the composition space Fe-9Cr-(0-1)Mo- (0-1)V-0.2C (wt.%) to be investigated. As the segregation ratios of Co and Ni are expected to be low based on the cast AerMet100 work [63], these constituents are excluded from the composition space to reduce the simulation time. The solidification simulations assume a cooling rate of  $0.5\text{ }^{\circ}\text{C s}^{-1}$ , a total solidification time of 1000 s, a secondary dendrite size of  $100\text{ }\mu\text{m}$  and no carbide precipitation. These assumptions are based on the results of the AerMet100 solidification study [63]. Tables 3-5 contain the calculated segregation ratios of the composition matrix studied. Figure 17 illustrates the effect of composition on the freezing range. Analysis of the predicted segregation ratio shows Mo to be the largest segregant. The addition of only Mo or V decrease Cr segregation. The additions of both Mo and V at high levels promote Cr segregation. V segregation increases with Mo additions. The freezing range increases with both Mo and V additions. Due to the large segregation ratio for Mo and the demonstrated ability to achieve a high  $M_2C$  driving force without Mo, Mo is removed from the design composition consideration. The first iteration design composition is then Fe-15Co-1.5Ni-9Cr-0.2V-0.2C (0.5C case) (wt.%).

Table 3. Matrix of the predicted  $\delta_{Cr}$  for Fe-9Cr-Mo-V-0.2C (wt.%) alloys

	0.0	0.5	1.0
0.0	1.56	1.50	1.51
0.2	1.49	1.51	-
0.5	1.50	1.52	1.54
1.0	-	1.55	-

*Table 4.* Matrix of the predicted  $\delta_{M_0}$  for Fe-9Cr-Mo-V-0.2C (wt.%) alloys

	0.0	0.5	1.0
0.0	–	2.51	2.56
0.2	–	2.55	–
0.5	–	2.61	2.67
1.0	–	2.72	–

*Table 5.* Matrix of the predicted  $\delta_V$  for Fe-9Cr-Mo-V-0.2C (wt.%) alloys

	0.0	0.5	1.0
0.0	–	–	–
0.2	1.75	1.79	–
0.5	1.79	1.84	1.88
1.0	–	1.94	–

#### 4.5. RE-OPTIMIZATION

Next, the first iteration composition is reexamined to insure self-consistency. Table 6 summarizes the predicted properties achieved by the first iteration composition. The strength is predicted for 50% completion of the  $M_2C$  precipitation reaction using the coherency model to determine the particle size input for the strengthening model [65]. The particle size is calculated assuming coherent carbides with an aspect ratio of 3, where this is the observed state just before coherency loss, corresponding typically to the peak hardness condition. The mole fraction of  $M_2C$  is set at 50% of the equilibrium value. An average coherent interfacial energy of  $120 \text{ mJ m}^{-2}$  is assumed. The strengthening mechanism is assumed to be dislocation by-pass and the modified Orowan theory was applied, Equation (4). The initial driving force for  $M_2C$  precipitation is slightly lower than the desired NASA1 driving force of 15.9 kJ/mole. Solution temperature constraints on the V solubility and Mo segregation during solidification restrict increasing the driving force of the alloy composition.

The Cr partitioning in the oxide film exceeds that of 440C, which has a value of  $y_{Cr} = 0.58$ . The pH-potential diagram for the alloy composition is shown in Fig. 18 and indicates that at the pH and electrode applied potential of interest (pH = 7 and potential range of  $(-0.1 \text{ to } 0.1 \text{ V, SHE})$ ) passivating oxides ( $Me_3O_4$  and  $Me_2O_3$ ) form. Note the alloy will enter a corrosive region if the pH is reduced to a pH less than 6 for potentials greater than  $-0.47 \text{ V, SHE}$ .

The initial composition possesses almost all of the desired properties. The calculated  $M_2C$  driving force for precipitation is 90% of the desired NASA1 value. This lower driving force is accepted as increasing the driving force would be done at the expense of other objectives. This completes the optimization of the design composition. To the design composition late boron and cesium additions are made at conventional levels during the vacuum-melt processing to improve grain boundary cohesion and getter impurities.

Table 6. Predicted properties of design prototype

Property	Value
<b>Case properties</b>	
$M_s$	446 K (172 °C)
Hardness at 50% completion	825 VHN
Final mole fraction $M_2C$	0.0668
Coherent $M_2C$ driving force at 482 °C	14.2 kJ/mole
Partitioning of Cr in oxide film, $y_{Cr}$	0.75
Solution Temperature, $T_s$	1100 °C
<b>Core properties</b>	
$M_s$	570 K (297 °C)
Hardness at 50% completion	575 VHN
final mole fraction $M_2C$	0.0282

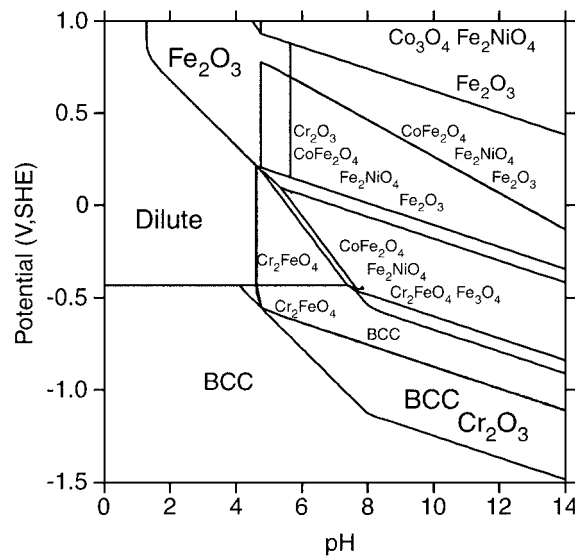


Figure 18. pH-potential diagram for Fe-15.5Co-1.5Ni-9Cr considering stoichiometric oxides.

## 5. Discussion

The presented computational design calculations represent the most recent work in the development of a martensitic secondary-hardening stainless steel. Previous design iterations for monolithic stainless steels and carburizable secondary-hardening gear steels directed the model development. The first iteration of this computational design process resulted in the design of the NASA1 prototype [68, 69]. While NASA1, a monolithic stainless bearing composition, was designed with somewhat limited design models, it achieved many of the desired design objectives and illustrated the feasibility of systems design. The weaknesses of the NASA1 composition highlighted the processing/structure/property interactions that required further model development. The greatest need was for further development of the model-

ing of the martensitic transformation behavior. With kinetic factors [46, 47] added to the modeling of the martensitic transformation behavior, the NASA2 prototype was designed. Characterization of NASA2 prototype showed improvement in obtaining the desired martensitic microstructure; however, the measured  $M_s$  temperature was still 150 deg below the desired  $M_s$  temperature indicating further model development was needed. Evaluation of the NASA2 prototype also showed that significant microsegregation had occurred with the high alloy concentration and implied that modeling of the solidification process would be useful. The C2 prototype [21, 70], a carburizing secondary-hardening alloy, was designed with approximate elastic strain energies added to the chemical thermodynamics of the  $M_2C$  carbide phase to account for coherency effects. This approximation underestimated the strengthening efficiency of the coherent  $M_2C$ ; thus, the current modeling incorporated SANS data on the particle size evolution to better calibrate the coherency strain energy and addressed the initial state of  $M_2C$  precipitation.

The current computational design of the carburizable secondary-hardening martensitic stainless steel incorporates refined models of the martensitic transformation behavior and the kinetics of the secondary-hardening process and adds models for the stability of the passivating film and the microsegregation resulting from solidification processing. Using these models, the present computational design predicts that an alloy composition with 9 wt.% Cr will provide more aqueous corrosion resistance than the 440C composition, which has 11 wt.% Cr in the matrix. The higher corrosion resistance for the lower Cr alloy is achieved by increasing the Cr activity in the matrix composition, and thus, increasing the Cr partitioning to the metastable oxide film. The design composition has a higher matrix Cr activity because of the large Co addition (15 wt.%) to obtain the desired martensitic microstructure. Avoiding the precipitation of primary carbides reduces the amount of Cr taken from the matrix composition.

## 6. Conclusions

A computational systems design approach determined property objectives for a new class of high-performance stainless steel, guided the development of mechanistic models, and determined a specific composition to meet the desired property objectives. To achieve the desired high fatigue strength, toughness, and aqueous corrosion resistance, a carburizing secondary-hardening, martensitic stainless steel requiring only thermal processing was conceived. The design was completed using the Thermo-Calc and DICTRA multicomponent thermodynamic and kinetic software packages to integrate models of the martensitic transformation behavior, coherent  $M_2C$  carbide precipitation, the formation and stability of passivating oxide films, and microsegregation resulting from solidification processing.

To complete the systems design process, the prototype must be characterized to determine if the desired microstructures are achieved and property objectives are met. The prototype characterization will also serve to determine strength and weaknesses of the models used. Evaluation of the prototype composition is discussed in part II [71].

## Acknowledgements

This research was supported by a NSF Graduate Fellowship for CEC and was conducted as part of the multi-institutional Steel Research Group program. The authors thank Dr G. Ghosh for assistance with the modeling of the martensitic transformation behavior. Pyrowear 675

was provided by Carpenter Technology. Alloy 1605-8A was produced by NKK Corporation, Japan.

## References

1. Olson, G. B., *Science*, 277 (1997) 1237.
2. Small, C. J. and Saunders, N., *MRS Bull.*, 24 (1999) 22.
3. Sundman, B. and Ågren, J., *MRS Bull.*, 24 (1999) 32.
4. Spear, K. E., Besmann, T. M. and Beahm, E. C., *MRS Bull.*, 24 (1999) 37.
5. Bernard, C., Pons, M., Blanquet, E. and Madar, R., *MRS Bull.*, 24 (1999) 27.
6. Villars, P., Onodera, N. and Iwata, S., *J. Alloys Compd.*, 279 (1998) 1.
7. Howe, A. A. and Farrugia, D. C. J., *Mater. Sci. Technol.*, 15 (1999) 15.
8. Spencer, P. J., *Thermochim. Acta*, 314 (1998) 1.
9. Olson, G. B., *Science*, 288 (2000) 993.
10. Jenkins, G. M., In Beishon, J. and Peters, G. (Eds.), *Systems Behavior*, Open University Press, Birmingham, UK, 1972, pp. 56-79.
11. Bamberger, E. N., In Loomis, W. R. (Eds.), *New Directions in Lubrication, Materials, Wear, and Surface Interactions: Tribology in the 80's*, Noyes Publications, 1983, pp. 736-756.
12. McCaffrey, T. J. and Wert, D. E., In Hoo, J. J. C. (Eds.), *Creative Use of Bearing Steels*, ASTM STP 1195, Vol. ASTM, Philadelphia, 1993, pp. 137-148.
13. Campbell, C. E., Doctoral dissertation, Northwestern University, Evanston, IL, 1997.
14. Morrow, J., *Internal Friction, Damping, and Cyclic Plasticity*, ASTM, 1964, pp. 45-84.
15. Basquin, O. H., *Proceedings, Am. Soc. Testing Mats.*, 1910, pp. 625-640.
16. Hornborgen, E. and Verpoort, C., In Francois, D. (Eds.), *Fifth International Conference on Fracture (1980)*, Pergamon Press Ltd., 1982, pp. 315-322.
17. Stoudt, M. R., Cammarata, R. C. and Ricker, R. E., *Scri Mater*, 43 (2000) 491.
18. Hengerer, F., Brockmüller, U. and Sörström, P. O., In Hoo, J. J. C. (Eds.), *Creative Use of Bearing Steels*, ASTM STP 1195, Vol. ASTM, Philadelphia, 1993, pp. 21-33.
19. Fontana, M. G., *Corrosion Engineering*, McGraw-Hill, New York, 1986.
20. Ashby, *Acta Metall.*, 37 (1989) 1273.
21. Kuehmann, C. J. and Olson, G. B., *Adv Mater Processes*, 153 (1998) 40.
22. Wise, J. P., Doctoral dissertation, Northwestern University, Evanston, IL, 1998.
23. Montgomery, J. S. and Olson, G. B., In Olson, G.B., Azrin, M. and Wright, E. S. (Eds.), *Innovations in Ultrahigh-Strength Steel in Technology (34th Sagamore Army Materials Research Conference)*, U.S. Government Printing Office, Washington DC, 1987, pp. 147-178.
24. Langer, J. S. and Schwartz, A. J., *Phys. Rev. A*, 21 (1980) 948.
25. Kampmann, R. and Wagner, R., In Haasen, P., Gerold, V., Wagner, R. and Ashby, M. F. (Eds.), *Decomposition of Alloys: the early stages*, 2nd Acta-Scripta Metallurgica Conference, Pergamon Press, 1983, pp. 91-103.
26. Speich, G. R., Dabkowski, D. S. and Porter, L. F., *Metall. Trans.*, 4 (1973) 303.
27. Kirchheim, R., *Electrochimica Acta*, 32 (1987) 1619.
28. Kirchheim, R., Heine, B., Fischmeister, H., Hofmann, S., Knote, H. and Stolz, U., *Corr. Sci.*, 29 (1989) 899.
29. Hall, A. M., *Nickel in Iron and Steel*, John Wiley & Sons, Inc., New York, 1954.
30. Jolley, W., *J. Iron Steel Inst.*, 206 (1968) 170.
31. Leslie, W. C., Sober, R. J., Babcock, S. G. and Green, S. J., *Trans. AMS*, 62 (1969) 690.
32. Olson, G. B., In G.B. Olson, M. Azrin and Wright, E. S. (Eds.), *Innovations in Ultrahigh-Strength Steel in Technology (34th Sagamore Army Materials Research Conference)*, U.S. Government Printing Office, Washington DC, 1987, pp. 3-66.
33. Schmidt, M. and Gore, M. J., In Olson, G.B., Azrin, M. and Wright, E. S. (Eds.), *Innovations in Ultrahigh-Strength Steel in Technology (34th Sagamore Army Materials Research Conference)*, U.S. Government Printing Office, Washington DC, 1987, pp. 407-424.
34. Kuehmann, C. J., Doctoral dissertation, Northwestern University, Evanston, IL, 1994.
35. Rice, J. R. and Wang, J.-S., *Mater. Sci. Eng.*, A107 (1989) 23.

36. Anderson, P. M., Wang, J. S. and Rice, J. R., In Olson, G. B., Azrin, M. and Wright, E. S. (Eds.), *Innovations in Ultrahigh-Strength Steel Technology*, Sagamore Army Materials Research Conference Proceedings, 1990, pp. 619-649.
37. Guttman, M., *Surf. Sci.*, 53 (1975) 213.
38. Waudby, P. E., *Int. Met. Rev.*, 2 (1978) 74.
39. Seah, M. P., Spencer, P. J. and Hondros, E. D., *Met. Sci.*, (1979) 307.
40. Garcia, C. I., Ratz, G. A., Burke, M. G. and DeArdo, A. J., *JOM*, (1985) 22.
41. Watton, J. F., Olson, G. B. and Cohen, M., In G.B. Olson, M.Azrin and Wright, E. S. (Eds.), *Innovations in Ultrahigh-Strength Steel in Technology (34th Sagamore Army Materials Research Conference)*, U.S. Government Printing Office, Washington DC, 1987, pp. 705-737.
42. Sundman, B., Jansson, B. and Andersson, J. O., *CALPHAD*, 9 (1985) 153.
43. Borgenstam, A., Engström, A., Höglund, L. and Ågren, J., *J. Phase Equil.*, 21 (2000) 269.
44. Olson, G. B. and Cohen, M., *Metall. Trans.*, 7A (1976) 1905.
45. Olson, G. B. and Cohen, M., *Metall. Trans.*, 7A (1976) 1915.
46. Ghosh, G. and Olson, G. B., *Acta Metall. Mater.*, 42 (1994) 3361.
47. Ghosh, G. and Olson, G. B., *Acta Metall. Mater.* 42 (1994) 3371.
48. SGTE, Scientific Group Thermochemica Europe, *Solution Database*, 1994.
49. Olson, G. B., Kinkus, T. J. and Montgomery, J. S., *Surf. Sci.*, 246 (1991) 238.
50. Allen, A. J., Gavillet, D. and Weertman, J. R., *Acta Metall. Mater.*, 41 (1992) 1869.
51. Montgomery, J. S. and Olson, G. B., In Krauss, G. and Repas, P. E. (Eds.), *Gilbert R. Speich Symp. Proc.: Fundamentals of Aging and Tempering in Bainitic and Martensitic Steel Products*, 1992, pp. 177-214.
52. Wagner, R. and Kampmann, R., In G.B. Olson, M.Azrin and Wright, E. S. (Eds.), *Innovations in Ultrahigh-Strength Steel in Technology (34th Sagamore Army Materials Research Conference)*, U.S. Government Printing Office, Washington DC, 1987, pp. 209-221.
53. Hultgren, A., *ASM*, 39 (1947) 915.
54. Hillert, M., *Acta Metall.*, 3 (1955) 34.
55. Hillert, M., In Bennett, L. H., Massalski, T. B. and Giessen, B. C. (Eds.), *Alloy Phase Diagrams: Materials Research Society Symposia Proceedings*, Elsevier Science Publishing, Co., 1983, pp. 295-309.
56. Hillert, M. and Ågren, J., In Embury, J. D. and Purdy, G. R. (Eds.), *Advances in Phase Transitions: International Symposium*, Pergamon Press, 1987, pp. 1-19.
57. Ghosh, G., Campbell, C. E. and Olson, G. B., *Metall. Mater. Trans.*, 30A (1999) 501.
58. Liarnng, R.-H., *Doctoral dissertation*, Northwestern University, Evanston, IL, 1996.
59. King, K. C., Voorhees, P. W., Olson, G. B. and Mura, T., *Metall. Trans.*, 22A (1991) 2199.
60. Johnson, W. C. and Cahn, J. W., *Acta Metall.*, 32 (1984) 1925.
61. Pourbaix, M., *Atlas of Equilibria in Aqueous Solution*, Pergamon, New York, 1966.
62. Craig, B. D., *Fundamental Aspects of Corrosion Films in Corrosion Science*, Plenum Press, New York, 1991.
63. Lippard, H. E., Campbell, C. E., Björklind, T., Borggren, U., Kellgren, P., Dravid, V. P. and Olson, G. B., *Metall. Mater. Transa.*, 29B (1998) 205.
64. Orowan, E., *Internal Stresses in Materials Alloys*, Institute of Metals, London, 1948.
65. Ashby, M. F., *Phil. Mag.*, 14 (1966) 1157.
66. Heine, R. W., Carl R. Loper, J. and Rosenthal, P. C., *Principles of Metal Casting*, McGraw-Hill Book Company, New York, 1967.
67. Dennsion, J. P. and Tull, E. V., *J. Inst. Metals*, 85 (1956) 1712.
68. Bilyk, A., *class report*, Northwestern University, Evanston, IL, 1989.
69. Olson, G. B., *U. S. Patent*, 5,221,372, 1993.
70. Cook, D. J. and Lewis, G. A., *Class reprot*, Northwestern University, Evanston, IL, 1994.
71. Campbell, C. E. and Olson, G. B., *J Comput-Aided Mater Des*, 2001.